Transactions of the Materials Research Society of Japan 29[5] 1977-1982 (2004)

Nanoscale Disequilibrium in Waste Form Apatites

T.J. White, Dong ZhiLi and J.Y. Kim
Centre for Advanced Research of Ecomaterials, Nanyang Technological University, Singapore.
Fax: 65-6792-1291, e-mail: tjwhite@ntu.edu.sg

The disequilibrium features of the simplified waste form apatites $(Pb_xCa_{10-x})(VO_4)_6(F_{2-2y}O_y\square_y)$ with $0<x<9$ and $0<y<0.5$ were studied by quantitative powder XRD and HRTEM supported by multislice simulation. Annealing times of more than 2 weeks were required to equilibrate the materials and stabilize calcium-lead partitioning over the available crystallographic sites. Nanoscale disorder imparts additional flexibility for apatites to respond to variations in waste stream composition.

Key words: nanostructure, crystal structure, apatite, disequilibrium, hazardous waste.

1. INTRODUCTION

Anthroprogenic toxic metal contamination is of concern at industrial, urban and mining localities worldwide, but the management of these wastes using thermal, biological and physical/chemical methods can be costly and time consuming. In the context of developing sustainable industrial practices it is preferable to view toxic metal wastes as raw material reserves capable of incorporation in secondary products. One method of transforming toxic metal-bearing materials into reusable resources is through geomimetic stabilization, in which wastes are converted into specific synthetic minerals, known to be stable over geological timescales in established geological settings [1]. Synthetic apatites are one class of materials being developed for fixation and recycling [2,3], especially for the treatment of lead-contaminated soils and waters [4,5]. Current research has focused on phosphate apatites although this structural family exhibits a diverse chemistry applicable to environmental technologies.

While the general crystal chemical formula of apatites is most often expressed as $[A^I_2][A^{II}_3](BO_4)_3X$, $[A_5](BO_5)_3X$ and $[A_5](BO_3)_3X$ derivatives are also known [6]. All three apatite-types adopt symmetries belonging to maximal non-isomorphic subgroups of $P6_3/mcm$ (193), the commonest being $P6_3/m$ (176). The A^I and A^{II} positions accept large, low valence cations while smaller metals and metalloids occupy the B site. The X anion site that is filled by halides, oxygen or hydroxyl may be highly nonstoichiometric. Apatites that can be adapted as ecomaterials include the type-mineral $(Ca_5(PO_4)_3(F,Cl,OH))$ [7], mimetite $(Pb_5(AsO_4)_3Cl)$ [8] and vanadinite $(Pb_5(VO_4)_3Cl)$ [9].

This report describes the synthesis of the fluoro-vanadinites $(Pb_xCa_{10-x})(VO_4)_6F_{2\delta}$, $0<x<9$, and compares and contrasts the crystal structure and local atomic order in equilibrated and non-equilibrated material. As eco-apatites are prepared under conditions that diverge greatly from thermodynamic or kinetic equilibrium an understanding of such features is particularly relevant to the validation of waste form performance. To date, there has been essentially no assessment of the impact of disequilibrium on stabilization capacity, an issue addressed in this study of a simplified waste form system.

2. EXPERIMENTAL METHODS

Ten fluoro-vanadinites of nominal compositions $(Pb_xCa_{10-x})(VO_4)_6F_2$ with $0<x<9$ were synthesized in air at 800°C by the solid state reaction of homogenized CaO, PbO, V_2O_5 and CaF_2 powders contained by alumina crucibles. Sintering and sampling continued at intervals of 10hr, 1w, 2w and 4w. In the case of $(Pb_5Ca_5)(VO_4)_6F_{2\delta}$ treatment was extended to 7 weeks. Subsequent data analysis showed that equilibration was achieved after annealing for >2w. The firing temperature was just below the melting point of the lead end-member $Pb_{10}(VO_4)_6F_2$.

Powder X-ray diffraction (XRD) patterns were collected with Cu Kα radiation at a power of 1.6 kW over the angular range 10 – 140 ° 2θ with a step size 0.01° and counting time of 5 seconds per step. Before collection, the fired agglomerates were reduced to fine powders and mixed with approximately 25 wt.% of standard silicon powder with a_0 = 5.43088Å (NIST 640c) to internally calibrate the zero shift. Rietveld analysis, based on the fundamental parameter method [10], was used for crystal structure refinement. A starting model took the atomic positions for $Ca_{10}(PO_4)_6F_2$ [11] with Ca/Pb occupancy set according to the bulk composition and equal partitioning of Pb and Ca over the A^I and A^{II} sites. The symmetry $P6_3/m$ was used for all compositions, although the calcium end member $Ca_{10}(VO_4)_6F_2$ is pseudo-hexagonal and monoclinic $P2_1/m$ [12]. Isotropic temperature factors for calcium, lead and vanadium were refined, but those for oxygen and fluorine were set at 1 $Å^2$. For the VO_4 tetrahedra a penalty function was used to constrain the V-O bond length close to 1.735Å. Calcium and lead occupancies were refined such that $N(Ca) + N(Pb) = 1$ was satisfied for A^I and A^{II} – less than 100% occupancy was not considered.

High resolution transmission electron microscopy (HRTEM) was conducted on powdered specimens using a JEM-3010 microscope (C_s = 1.2 mm) operated at 300kV with images recorded from the [0001] zone axis. Simulated micrographs were calculated by the multislice method [13] using as a starting point the structures determined by XRD refinement. Digital filtering and tests for local symmetry were carried out using Fourier filtering methods as implemented in CRISP [14].

Table I: Refined crystal and atomic parameters for vanadinite annealed at 800°C for intervals from 10 hr to 7 weeks.

Time/Parameter	10 hr	1 week	2 weeks	7 weeks
Composition	$(Pb_{4.62}Ca_{5.38})(VO_4)_6F_2$	$(Pb_{4.90}Ca_{5.10})(VO_4)_6(F_{0.6}O_{0.7})$	$(Pb_{4.78}Ca_{5.22})(VO_4)_6(F_{0.6}O_{0.7})$	$(Pb_{4.76}Ca_{5.64})(VO_4)_6(F_{0.6}O_{0.7})$
Crystal Formula	$[Pb_{1.56}Ca_{2.44}][Pb_{2.06}Ca_{2.94}](VO_4)_6F_2$	$[Pb_{1.12}Ca_{2.88}][Pb_{3.78}Ca_{2.22}](VO_4)_6(F_{0.3}O_{0.7})$	$[Pb_{0.64}Ca_{3.36}][Pb_{4.14}Ca_{1.96}](VO_4)_6(F_{0.25}O_{0.75})$	$[Pb_{0.68}Ca_{3.32}][Pb_{4.08}Ca_{1.92}](VO_4)_6(F_{0.3}O_{0.7})$
a (Å)	9.9462(1)	10.0011(1)	10.0025(2)	10.0124(2)
c (Å)	7.1983(1)	7.1993(1)	7.1858(1)	7.1880(1)
Volume (Å^3)	616.7	623.6	622.6	624.0
c/a	0.7237	0.7199	0.7184	0.7179
N(Ca1)	0.61	0.72	0.84	0.83
N(Ca2)	0.49	0.37	0.31	0.32
$k_{Pb}(A^I/A^{II})$[b]	0.52	0.30	0.16	0.17
ϕ (°)	$22._0$	$16._1$	$14._5$	$14._4$
z(A1)	0.0095(8)	0.0083(8)	0.0062(11)	0.0059(12)
B(A1)	0.6	1.2	0.4	1.4
x(A2)	0.2427(3)	0.2442(2)	0.2418(2)	0.2426(2)
y(A2)	0.0023(4)	0.0028(3)	0.0026(3)	0.0036(3)
B(A2)	0.6	1.1	1.3	1.7
x(V)	0.4020(7)	0.4066(5)	0.4090(6)	0.4093(6)
y(V)	0.3758(6)	0.3770(5)	0.3813(6)	0.3805(6)
B(V)	0.3	0.2	0.2	0.6
x(O1)	0.3195(18)	0.3363(16)	0.3407(17)	0.3393(18)
y(O1)	0.4915(18)	0.5014(16)	0.5073(16)	0.5057(17)
x(O2)	0.6012(20)	0.6046(19)	0.6056(20)	0.6074(20)
y(O2)	0.4755(18)	0.4782(16)	0.4787(17)	0.4807(17)
x(O3)	0.3353(13)	0.3436(10)	0.3545(10)	0.3499(11)
y(O3)	0.2546(13)	0.2594(11)	0.2635(11)	0.2639(12)
z(O3)	0.0628(13)	0.0602(13)	0.0605(13)	0.0583(14)
N(F)	1.0	0.6	0.5	0.6
R_b (%)[a]	4.2	4.4	5.0	4.9

[a] $R_b = \frac{\sum_i |I_{ko} - I_{kc}|}{\sum_i I_{ko}}$

[b] $k_{Pb}(A^I/A^{II}) = (2\text{-}2N(Ca1))/(3\text{-}3N(Ca2))$. For equal partitioning of Pb over A^I and A^{II} $K_{Pb} = 0.66$.

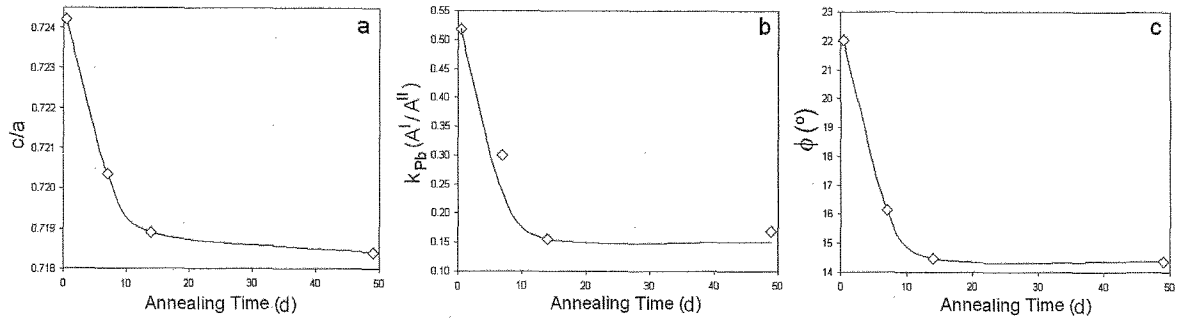

Fig. 1. Correlation of (a) *c/a* cell parameter ratio, (b) lead partitioning co-efficient k_{Pb}, and (c) A^IO_6 metaprism twist angle (ϕ) in $(Pb_5Ca_5)(VO_4)_6(F_{2-2y}O_y\square_y)$ as a function of annealing time at 800°C in air.

3. RESULTS

3.1 Crystal structure refinement

For '$Pb_5Ca_5(VO_4)_6F_2$' crystal structures were refined after 10hr, 1w, 2w and 7w annealing. A portion of the refined data are summarized in Table I. As annealing progresses the *c/a* lattice constant ratio decreases exponentially such that equilibrium is approached only after 30 days annealing (Fig. 1a). Concomitant with this adjustment is the enrichment of lead in the A^{II} position (Fig. 1b) and a decrease in the A^IO_6 metaprism twist angle (ϕ) (Fig. 1c). Fully equilibrated vanadinite that was heat treated for 7w had a substantially smaller $k_{Pb}(A^I/A^{II})$ of 0.17 as compared to 0.52 for 10 hr material, and ϕ reduced to $14._4°$ from $22._0°$.* As annealing progressed fluorine was slowly oxidized such that $2F^- \rightarrow O^{2-}$ and the material is more correctly described as $(Pb_5Ca_5)(VO_4)_6(F_{2-2y}O_y\square_y)$

3.1 Variation in cell constants

While unit cell parameters dilate as lead (effective ionic radii = 1.29Å for VIII co-ordination) replaces calcium (1.12Å), neither equilibrated nor non-equilibrated apatites obeyed Vergard's Law across the entire compositional range from 0<x<1 (Fig. 2). Rather, the cell constants were best described as two linear segments such that after 10hr annealing

$$a = 9.707 + 0.469x \quad \text{for } 0<x<1 \quad (1)$$

and

$$c = 7.015 + 0.309x \quad \text{for } 0<x<0.3 \quad (2a)$$
$$c = 7.459 - 0.521(1-x) \quad \text{for } 0.4<x<1 \quad (2b)$$

while heat treatment for 4w yielded

$$a = 9.737 + 0.587x \quad \text{for } 0<x<0.5 \quad (3a)$$
$$a = 10.108 - 0.189(1-x) \quad \text{for } 0.6<x<1 \quad (3b)$$

and

$$c = 7.006 + 0.382x \quad \text{for } 0<x<0.5 \quad (4a)$$
$$c = 7.420 - 0.399(1-x) \quad \text{for } 0.6<x<1 \quad (4b)$$

* The derivation of metaprism twist angle (ϕ) and the method of calculation is given by White & Dong [6].

3.3 Nanoscale disorder

Vanadinite powders were prepared for microscopy by deposition of alcohol suspensions on holey carbon films supported by copper grids. HRTEM images were collected from $(Pb_5Ca_5)(VO_4)_6F_{2\delta}$ thin crystal wedges annealed for 10 hr and 7 w. After short heat treatment [0001] micrographs possessed mottled contrast indicative of short-range disorder while long sintering yielded crystals with periodic contrast (Fig. 3).

Fourier processing of regions A and B in the disordered [0001] crystal images yielded potential maps with similar figures of merit ($R_{amplitudes}$ and φ_{res}) when the plane space group symmetries *p6* (consistent with space groups $P6_3/m$, $P6_3$, P-3, $P2_1/m$) or *p3* (P-6) were applied. The high symmetry space group $P6_3/m$ is considered correct for these nanodomains and is consistent with the XRD refinements.

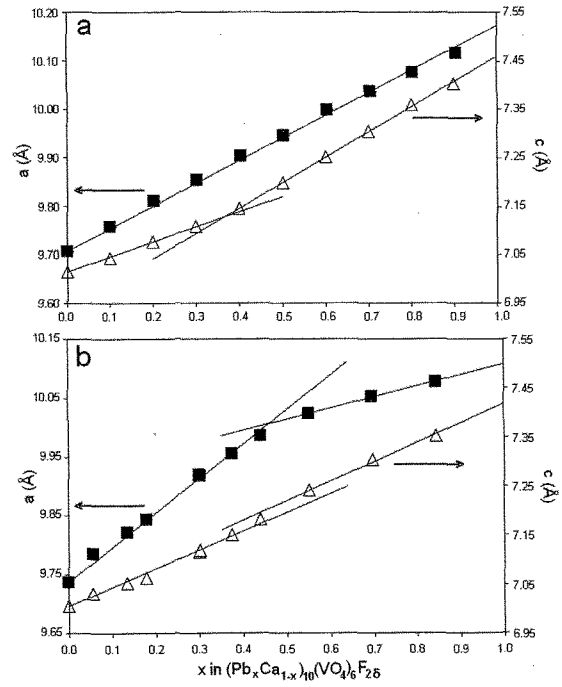

Fig. 2. Variation in cell constants for vanadinites of composition $(Pb_xCa_{1-x})_{10}(VO_4)_6F_{2\delta}$ when in (a) disequilibrium after 10hr annealing and (b) in equilibrium after 4 w annealing.

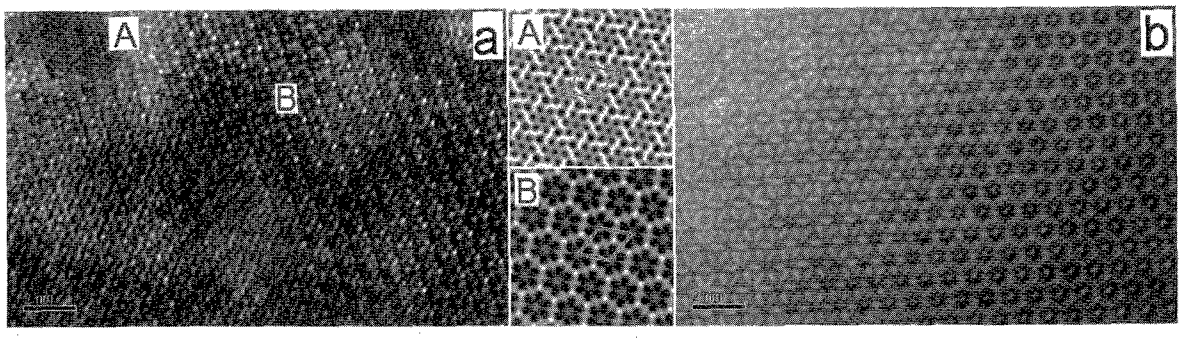

Fig 3. Comparison of high resolution transmission electron micrographs collected in the [0001] orientation from $(Pb_5Ca_5)(VO_4)_6F_{2\delta}$ annealed for (a) 10h and (b) 7w. Unit cell scale disequilibrium, evident in the crystal heat-treated for 10h arises from local variation in K_{Pb}, while longer sintering yields highly regular contrast indicative of equilibration and more perfect Ca/Pb ordering. Fourier treatment of regions 'A' and 'B' in (a) using the constraint of *p6* planar symmetry lead to quite different reconstructed electron potential maps.

4. DISCUSSION

4.1 Twist angle (ϕ) as a probe for disequilibrium

The fluoro-vanadinites are derived from triangular anion nets between which cations are periodically inserted to form A^IO_6 metaprisms, BO_4 tetrahedra and $A^{II}O_6X$ polyhedra – in this instance $(Ca,Pb)O_6$, VO_4, and $(Ca,Pb)O_6F$. By including metaprisms and tetrahedra in structure drawings systematic changes in crystal chemistry and topology are readily monitored (Fig. 4). This description also highlights the channel structure of apatite. As the channels are constructed of corner connected metaprisms and tetrahedra, the cavity is flexible, expanding and contracting to accommodate larger or smaller ions. If the atomic occupancy of the tunnel is reduced, or larger cations are progressively replaced by smaller cations, then collapse takes place through increased twisting (larger ϕ) of the metaprisms. Consequently, the metaprism twist angle is exceedingly sensitive to changes in the contents of the apatite channel.

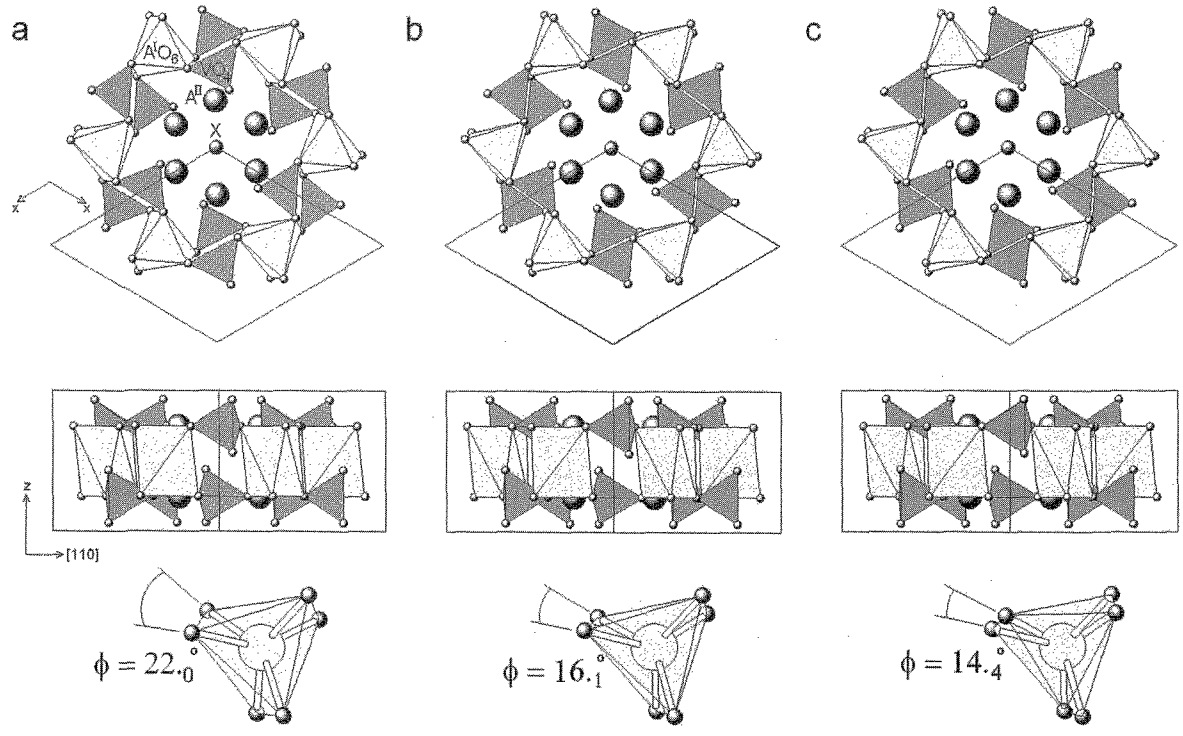

Fig 4. The crystal structures of the fluoro-vanadinites (a) $[Pb_{1.56}Ca_{2.44}][Pb_{2.06}Ca_{2.94}](VO_4)_6F_2$ with refined x = 4.62 (b) $[Pb_{0.64}Ca_{3.36}][Pb_{4.14}Ca_{1.96}](VO_4)_6(F_{0.25}O_{0.75})$ with x = 4.78 and (c) $[Pb_{0.68}Ca_{3.32}][Pb_{4.08}Ca_{1.92}](VO_4)_6(F_{0.3}O_{0.7})$ with x = 4.76 synthesized from stock powders but annealed respectively for 10hr, 2w and 7w at 800°C. In the upper portion of the drawing the A^IO_6 metaprisms and VO_4 tetrahedra are emphasized in [0001] projection. Through corner-connection these polyhedra form large channels that accommodate A^{II} cations and X anions. As A^{II} becomes progressively lead-rich the channel opens through A-O bond dilation and a reduction of metaprism twist angle (ϕ).

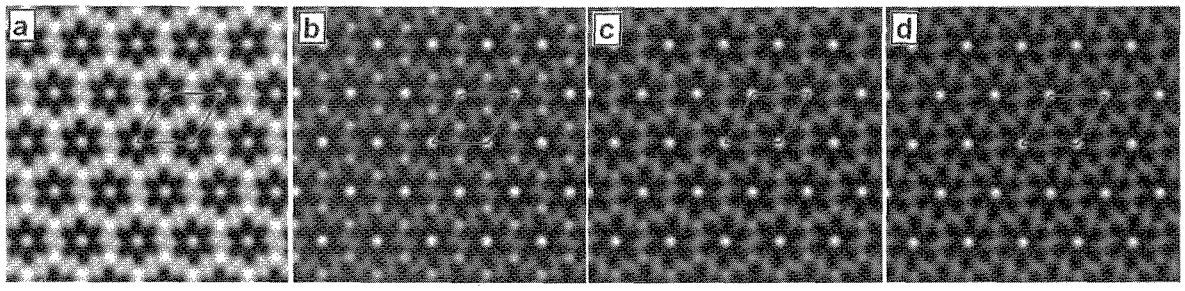

Fig. 5. Comparison of (a) a reconstructed electron potential map for equilibrated vanadinite (derived from Fig. 3b using p6 planar symmetry) and (b)-(d) multislice simulated images having a range of $k_{Pb}(A^I/A^{II})$. Calculations were made for t =8.3nm and Δf = –10nm for vanadinites with (b) x = 0.50, k_{Pb} = 0.67 (equal partitioning of Pb and Ca over the A^I and A^{II} sites), (c) x = 0.51, k_{Pb} = 0.31 and (d) x = 0.51, k_{Pb} = 0.16. This progression of k_{Pb} simulates crystallochemical equilibration that takes place during annealing. Contrast varies as a function of k_{Pb} and is of sufficient magnitude to distinguish adjacent region of different composition by HRTEM. Quantitative analysis of these contrast differences to derive k_{Pb} directly from the high resolution images was not possible.

This sensitivity of ϕ to compositional variations can be used to track crystal chemical adjustments accompanying annealing of $(Pb_5Ca_5)(VO_4)_6(F_{2-2y}O_y\square_y)$ vanadinite. At short annealing times, near equilibrium partitioning of lead over the A^I and A^{II} is not established, but rather $K_{Pb}(A^I/A^{II})$ = 0.52 which approaches almost even distribution of lead over these sites. However, after 7 w annealing, lead is substantially ejected from the smaller A^I site and K_{Pb} is reduced to 0.17. Conversely, this implies the vanadinite channel provides the preferred host sites for larger lead ions, which can only be accommodated by opening the cavity through reduction of ϕ. Indeed, in passing from the disequilibrium to equilibrium condition, ϕ decreases by 35%.

4.2 Systematization of variations in cell constants

For vanadinite in disequilibrium *a* varied linearly across the entire compositional range (see equation (1)) in near compliance with Vergard's Law implying that substitution of lead over the A^I and A^{II} sites was not strongly-differentiated.

As lead content increases the vanadinite channel enlarges, partially through satisfying the need for longer A^I-O and A^{II}-O bond lengths, and also by reduction in ϕ as noted above. It has been shown elsewhere [11] that for any apatite solid solution series *a* may be related to ϕ through a simple geometrical relationship, and that where *a* varies linearly, the rate of change of ϕ with composition is constant. Because all substantial structural adjustments take place in the (0001) plane the *c* parameter behaves in a simpler fashion than *a*.

At equilibrium, differentiation of lead partitioning causes the *a* cell edge to adjust according to equations (3a) and (3b) with a dramatic inflection occurring for x~0.45 (Fig. 2). This can be understood by considering that vanadinite contains 4 A^I sites (the preferred location of Ca) and 6 A^{II} sites (favoured by Pb). Thus, if there were perfect discrimination by Pb and Ca over these sites a vanadinite with x=0.6 of composition $[Ca_4][Pb_6](VO_4)_6X_2$ would crystallize. The change in the slope of *a* reflects a change in partitioning mechanism probably due to lead being strongly excluded from the A^I beyond x = 0.45.

4.3 Direct observation of disequilibrium

Some care is required when studying cation order-disorder in apatites by HRTEM as etching and amorphisation can proceed rapidly unless low electron fluxes and/or cooled specimen stages are used [15]. Moreover, the structure of apatite is relatively complex, and without the benefit of a short (~3Å) crystallographic projection providing an unobscured view of homoatomic cation columns, intuitive interpretation of HRTEM images is impossible.

In a parallel investigation [16] it has been shown that lead vanadinite can transform to single crystal $CaVO_3$ perovskite under intense electron irradiation as produced in a field emission TEM. However, using the relatively gentle conditions of a LaB_6 source, long working times (well in excess of those possible with hydroxyapatite *HAp*) are feasible. Therefore, the nanodomain images shown in Fig. 3a can be ascribed to local changes in composition, and in particular, to variation in the Ca/Pb ratio. This interpretation is supported by the fact that similar images collected from equilibrated vanadinite failed to display the same complex nanostructure (Fig. 3b).

In the specific case of lead substitution in *HAp*, calculations by Brès *et al.* [17] suggested that microchemical ordering over the A^I and A^{II} sites may be recognised in thicker crystals when viewed along [2-110] with a 400keV microscope. Our calculations of [0001] thickness-defocus wedges in which x ~ 5, but k_{Pb} varies from 0.67 to 0.17, suggests that unit-cell scale fluctuations in Ca/Pb partitioning will be detectable as subtle changes in image contrast. (A portion of an extensive set of multislice simulations is show in Fig. 5.) This is consistent with our experimental observations (Fig. 3a) where compositionally discrete nanodomains were the dominant feature of non-equilibrated vanadinite. Although the gross features of the processed and simulated images agree reasonably well it was not possible with resolution available to differentiate quantitatively A-cation ordering. Furthermore, although image processing constrained the electron potential maps to p6 symmetry, the presence of local regions with lower symmetry in the non-equilibrated apatites cannot be ruled out.

5. CONCLUSION

A combination of powder X-ray diffraction and high resolution transmission electron microscopy have demonstrated that long annealing times of several weeks are necessary to completely equilibrate calcium-lead partitioning in $(Pb_xCa_{10-x})(VO_4)_6F_{2\delta}$ with $0<x<9$ vanadinite apatite. These results provide a useful baseline for predicting the behavior of waste form apatites, which in actual use, will be fabricated using short firing times (less than 15 minutes) or through rapid precipitation. In both instances, the apatites will be far from equilibrium, and in those cases where chemically complex waste is to be immobilized, will exhibit complex microstructures.

Often apatites are regarded as suitable hosts for hazardous waste on the basis of the stability of analogous natural minerals that have equilibrated over geological timescales. It is presently unclear if similar long-term chemical durability will be demonstrated by synthetic apatites. It is however noteworthy, that parallel work in our laboratory on gem quality apatites has shown the co-existence of ellestadite (a sulfo-silicate apatite) and fluoroapatite at the scale of a few hundred angstroms suggesting that nanophase separation may be a useful feature for apatites to respond flexibly to changes in waste stream composition.

Acknowledgement
Supported through ASTAR Grant 012 105 0123.

References

[1] H. Pöllmann, "Mineral Reservoirs for Immobilisation Purposes of Hazardous Materials" in Advances in Environmental Materials, Vol. II Environmentally Preferred Materials, edited by T.J. White & J.A. Stegemann, Materials Research Society, Singapore (2001). pp. 317-330.
[2] Z.L. Dong, T.J. White, B. Wei and K. Laursen, *J. Am. Ceram. Soc.* **85**, 2515-2533 (2002).
[3] T.A. Ioannidis and A.I. Zouboulis, *J. Hazard. Mater.* **B97**, 173-191 (2003).
[4] P. Zhang and J.A. Ryan, J.A. *Environ. Sci. Technol.* **33**, 625-630 (1999).
[5] J. Jeanjean, U. Vincent and M. Fedoroff, *J. Solid State Chem.* **108**, 68-72 (1994).
[6] T.J. White and Z.L. Dong, *Acta Cryst.* B**59**, 1-16 (2003).
[7] J.Y. Kim, R.R. Fenton, B.A. Hunter, and B.J. Kennedy, *Aust. J. Chem.* **53**, 679-686 (2000).
[8] N.J. Calos and C.H.L. Kennard, *Z. Kristallogr.* **191**, 125-129 (1990).
[9] Y-S. Dai and J.M. Hughes, *Can. Mineral.* **27**, 189-192 (1989).
[10] R.W. Cheary and A.A. Coelho, *J. Appl. Cryst.* **31**, 851-861 (1998).
[11] K. Sudarsanan, P.E. Mackie and R.A. Young, *Mat. Res. Bull.* **7**, 1331-1338 (1972).
[12] Z.L. Dong and T.J. White, *Acta Crystallogr.,* B, submitted (2003).
[13] P.A. Stadelmann, *Ultramicroscopy* **21**, 131-146 (1987).
[14] X. Zou, M. Sundberg, M. Larine and S. Hovmoller, Ultramicroscopy, **62**, 103-121 (1996).
[15] K. Sato, T. Kogure, H. Iwai and J. Tanaka,. *J. Am. Ceram. Soc.* **85**, 3054-3058 (2002).
[16] Z.L. Dong, K. Sun, L.M. Wang, T.J. White and R.C. Ewing *J. Am. Ceram. Soc.* submitted (2003).
[17] E.F. Brès, J.C. Voegel, J. C. Barry, W.G. Waddington and R.M. Frank, R. M. *J. Appl. Cryst.* **19**, 168-173 (1986).

(Received October 10, 2003; Accepted October 31, 2003)